

The Role of Gravity Waves in the MLT Inversion Layers over Low-Latitude Using SABER Satellite Observations

Chalachew Lingerew^{1*}, U. Jaya Prakash Raju¹

¹Department of Physics, Washera Geospace, and Radar Science Laboratory, Bahir Dar University, Bahir Dar, Ethiopia

Correspondence to: Chalachew Lingerew (chalachewlingerew@gmail.com)

Abstract

The Mesosphere transitional region is a distinct and highly turbulent zone of the atmosphere. A transition mesosphere region is connected with dynamic processes, particularly gravity waves, as a causative of an inversion phenomenon. Understanding MIL (mesosphere inversion layer) phenomena is important under the influence of atmospheric waves for the understanding of middle and upper atmosphere dynamics for two primary reasons: stability and energy transfer. Mesospheric inversions have been the subject of numerous investigations, but their formation mechanisms are still poorly understood. In this article, an attempt has been made to investigate the upper and lower inversion phenomena and their causative mechanisms using long-term SABER observations in the height range of 60-100 km from 2005 to 2020 over a low-latitude region (3-15° N). The results indicate that the frequency of occurrence rate for the upper inversion is below 40%, whereas for the lower inversion, it is below 20%, indicating that the upper inversion is dominant over the lower inversion. The upper inversion exists in the height range of 78-91 km with an inversion amplitude of ~20-80 k and a thickness of ~3-12 km, whereas the lower inversion is confined in the height range of 70-80 km with an inversion amplitude of ~10-60 k and a thickness of ~4-10 km. Therein the gravity wave indicator potential energy depicts high energy (below 100 J/kg) in the upper mesosphere region (85 and 90 km) compared to the lower mesosphere region (70 and 75 km) with less than 50 J/kg. On account of Gws, the stability criteria from Brunt-Vaisala frequency (N^2) indicate instability in the upper mesosphere region with very low values relative to the lower mesosphere region. This result leads us to the conclusion that a high amount of gravity wave potential energy is a consequence of the high instability in the upper inversion relative to the lower inversion.

Keywords. MLT, Upper and Lower Inversions, Perturbed temperature, Causative gravity waves, Potential Energy, Brunt-Vaisala frequency, Instability.

31 **Introduction**

32 The mesosphere dynamic regions act as a transition zone to the lower and upper atmospheric wave
33 processes (tidal waves, planetary waves, and gravity waves). It is a well-known fact that
34 atmospheric waves, especially gravity waves (GWs) generated from the lower atmosphere,
35 propagate into the middle and upper atmospheres, break in the mesosphere region during
36 propagation, and dissipate their energy and momentum into the background atmosphere,
37 influencing the dynamics of the mesosphere thermal structure, global atmospheric circulation,
38 variability, and even the MIL phenomenon (Lindzen, 1981; Holton, 1983). The mesospheric
39 inversion layers (MILs) are a common feature that appeared to increase the mesosphere
40 temperature variability. The MIL is a symptom (sign) of wave saturation in the mesosphere when
41 the lapse rate is less than half of the dry adiabatic lapse rate (Sica et al., 2007). Temperature
42 inversions have been omnipresent features in the mesosphere regions for decades, and they have
43 been comprehensively studied in the past by using all sorts of available techniques (e.g., lidar,
44 radar, rocket sonde, and satellite) over different geographic locations.

45 Because of gravity waves (GWs) momentum and energy deposition, it is thought to be the principal
46 mechanism driving large-scale circulation and coupling of distinct atmospheric layers, as well as
47 inversion phenomena (Fritts and Alexander, 2003; Lindzen, 1981; Smith, 2012). In addition, the
48 gravity wave-breaking influence on mesosphere dynamics is an attempt to demonstrate the
49 emergence of the inversion phenomenon over mid and high latitudes (Gan et al., 2012;
50 Walterscheid and Hickey, 2009; Collins et al., 2011; Szewczyk et al., 2013). Observational and
51 modeling approaches have been used to investigate GWs as the causative of inversions (Fritts,
52 2018; Collins et al., 2014; Sridharan et al., 2008; Ramesh and Sridharan, 2012; Ramesh et al.,
53 2013, 2014, 2017). The effect of gravity waves in the mesosphere inversion based on temperature
54 variability is studied particularly over the mid- and high-latitudes (Singh and Pallamraju, 2018;
55 Fritts et al., 2018). As a result, the inversion phenomenon has been the topic of numerous studies
56 in mesosphere dynamics, yet the mechanisms of development have been poorly understood.

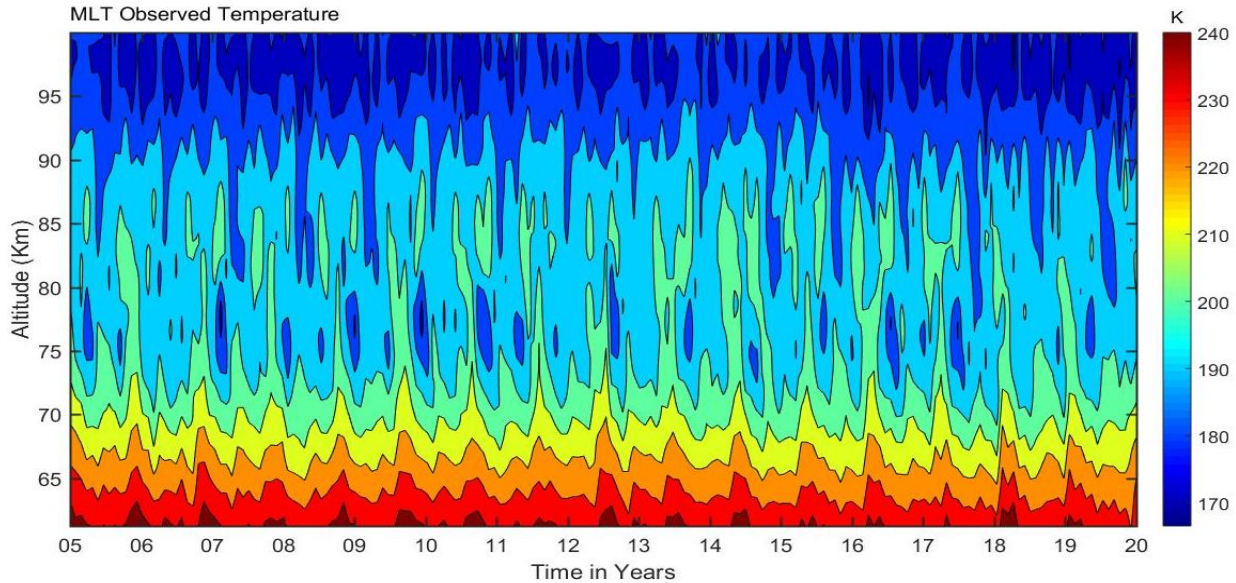
57 MILs are actual geophysical phenomena, and the study of MILs is important for a full
58 understanding of the structure and dynamics of the MLT parts of the upper atmosphere
59 (Meriwether and Gardner, 2000; Meriwether and Gerrard, 2004). Regarding the low latitudes,
60 there are very less number of studies on the temporal (time) and spatial (altitudinal, latitudinal, and
61 longitudinal) variability of the mesosphere inversion phenomenon associated with gravity wave

62 activity. This motivates us to investigate the mesosphere inversion phenomenon and its association
63 with gravity wave activity, along with stability criteria using Brunt-Vaisala frequency (N^2) over
64 the low latitudinal band (3-15° N) using long-term SABER observations during 2005-2020. This
65 is organized as follows: The data and method of extracting the mesosphere inversion phenomenon
66 are presented in Section 2, and their results are described in Section 3. Finally, Section 4 presents
67 the conclusions.

68 **2. Observation and Data analysis**

69 **2.1 SABER Observation**

70 The TIMED/SABER satellite was launched on December 7, 2001, to set on an elliptical orbit at
71 an altitude of about 625 km with an inclination of 74° from the equator. The SABER instrument
72 makes 15 orbits; each orbit takes 97 minutes (1.6 h) and provides about 1400 profiles **per day**; each
73 profile takes 58 seconds. This TIMED/SABER satellite provides temperature profiles with good
74 spatial and temporal resolution to investigate mesosphere dynamics and their atmospheric wave
75 processes. **SABER temperature data has been widely used to investigate the typical thermal**
76 **structure and dominant dynamical processes in the mesospheric region (Garcia et al., 2008, Gan et**
77 **al., 2012, 2014; Bizuneh et al., 2022; Lingerew et al., 2023). For vertical temperature**
78 **measurement, SABER provides an accuracy of 1 to 2 K between 15 and 60 km, decreasing to 5 K**
79 **below 85 km, while the error increases with altitude from 6.7 K to 10 K near 100 km (Rezac et al.,**
80 **2015). In the current work, we have used the latest version 2.0 of SABER observed temperature**
81 **data over low latitudes. The SABER vertical temperature profiles in the region of 60-100 km**
82 **altitude during the period January 2005-December 2020 over (3-15°N) latitude and (33-48°E)**
83 **longitude regions are used. Based on the monthly mean SABER profile data the mesosphere and**
84 **lower thermosphere (MLT) variability is presented, as shown in Figure 1. The monthly mean**
85 **temperature of the mesosphere region (60-100 km) shows a maximum temperature of 200-240 K**
86 **in the height range of 60-70 km, with the minimum temperature declining to around 160-180 K in**
87 **the height range of about 95-100 km throughout all over the period.**



88

89 **Figure 1.** The monthly mean MLT temperature variability in the height range of 60-100 km during
 90 December 2005-January 2020 over the low-latitude.

91 **2.2 Analysis Technique**

92 Mesosphere inversions of temperature are identified based on their characteristics thickness, and
 93 amplitude corresponding to an altitude and temperature difference between the top and bottom
 94 levels. In this investigation, the upper and lower mesosphere inversions are identified using the
 95 following criteria: (1) The bottom level of the lower and upper inversions is above 70 and 80 km,
 96 and its top level of inversion is below 80 and 92 km, respectively; (2) the amplitude is considered
 97 larger than 5 K; and (3) the thickness is greater than or equal to 2 km following the procedure. As
 98 well as identifying the inversions based on the above criteria, the upper and lower MLT inversion
 99 occurrence rate or percentage is derived by counting the number of inversion days in every month
 100 from 2005 to 2020. Inversions that satisfy the above-mentioned criteria are considered significant.
 101 Based on this sequence of temperature inversion, diagnostic techniques provided in the
 102 methodology (e.g. Gan et al., 2012 and Sivakandan et al. 2014) were applied to the SABER
 103 observed data during the period 2005-2020 over low latitudes to investigate the causative influence
 104 atmospheric gravity waves (Gws). This inversion of the mesosphere temperatures is related to their
 105 instabilities. Hence, we are going to derive the hourly atmospheric gravity waves via the Brunt-
 106 Vaisala frequency (N^2).

107 Another important concept to estimate the Brunt-Vaisala frequency is the potential temperature
 108 (θ), which stands for the air parcel's temperature when it is displaced adiabatically to a standard
 109 pressure level, p_0 , from the current pressure level, p , based on the first law of thermodynamics:

$$110 \quad \frac{dT}{T} = \frac{R}{c_p} \frac{dp}{p} \Rightarrow \int_T^0 \frac{dT}{T} = \int_p^{p_0} \frac{R}{c_p} \frac{dp}{p} \quad (1) \text{ it yields}$$

$$111 \quad \theta = T \left(\frac{p_0}{p} \right)^{R/c_p} \quad (2)$$

112 Therefore, the motion of the vertical atmospheric air parcel can be described by (Liu, 2011; Vadas
 113 and Fritts, 2005) as follows in equation (2.3) to calculate the Brunt-Vaisala frequency of the parcel
 114 due to the Buoyant and gravitational forces acting on the parcel:

$$115 \quad \frac{d^2s}{dt^2} = -g \frac{\rho - \rho_0}{\rho} \sin a \quad (3)$$

116 Based on the hydrostatic equation, $\rho = \rho_0$, and $p = p_0 \Rightarrow \frac{\partial p}{\partial z} = \frac{\partial p_0}{\partial z} = -g\rho_0$ (4) and the ideal gas
 117 law, $\rho = p/RT = p_0/RT$ gives the parcels motion of an equation:

$$118 \quad \frac{d^2s}{dt^2} = -\frac{g}{\rho} \left(\frac{d\rho}{dp} \frac{\partial p_0}{\partial z} - \frac{\partial \rho_0}{\partial z} \right) z \quad (5)$$

119 Following the same approach using the hydrostatic equation (4) and adiabatic equation (6)

$$120 \quad d \ln \rho = \frac{d \ln p}{\gamma}, \gamma = c_p/c_v \quad (6) \text{ yields}$$

$$121 \quad \frac{d^2s}{dt^2} = -\frac{g}{\rho} \left(\frac{\rho}{\gamma p_0} \frac{\partial p_0}{\partial z} - \frac{\partial \rho_0}{\partial z} \right) z = g \left(\frac{\partial \ln \rho_0}{\partial z} - \frac{1}{\gamma} \frac{\partial \ln p_0}{\partial z} \right) z \quad (7)$$

123 For the ideal gas law of $p = \rho RT$, the natural logarithm is taken for altitude, z on both sides, yielding

$$124 \quad \frac{\partial \ln \rho}{\partial z} = \frac{\partial \ln p}{\partial z} - \frac{\partial \ln T}{\partial z} \quad (8)$$

125 Then after, the potential temperature (θ) of the atmospheric parcel is calculated as follows based
 126 on the equation (2):

$$127 \quad \frac{\partial \ln \theta}{\partial z} = \frac{\partial \ln T}{\partial z} - \frac{R}{c_p} \frac{\partial \ln p}{\partial z} = \frac{1}{T} \left(\frac{\partial T}{\partial z} + \frac{g}{c_p} \right) = \left(1 - \frac{R}{c_p} \right) \frac{\partial \ln p}{\partial z} - \frac{\partial \ln \rho}{\partial z} \quad (9) \text{ to derive the}$$

128 Parcels acceleration based on equations (7) to become:

$$129 \quad \frac{d^2s}{dt^2} = -g \frac{\partial \ln \theta_0}{\partial z} z \sin a = -g \frac{\partial \ln \theta_0}{\partial z} ds \cdot \sin^2 a \quad (10)$$

130 Whereas by introducing the frequency, N , with $N^2 = g \frac{\partial \ln \theta_0}{\partial z}$

131 The Brunt-Vaisala frequency, N^2 is calculated based on the following mathematical formulation
 132 used to characterize atmospheric stability.

133
$$N^2(z) = \frac{g(z)}{T_0(z)} \left(\frac{\partial T_0(z)}{\partial z} + \Gamma_d \right) \quad (11)$$

134 Where g is the acceleration due to gravity, N is the Vaisala frequency, T_0 is the background
 135 temperature, estimated based on the third-order polynomial fitting, $\Gamma_d = \frac{g}{c_p}$ is the adiabatic lapse
 136 rate, and $c_p = 1004 J K^{-1} kg^{-1}$ is the specific heat capacity of the atmosphere at constant
 137 pressure. When Vaisala frequency N^2 , is statically positive, the atmosphere is stable. While the
 138 frequency N^2 , is negative, the atmosphere is unstable, in which the atmospheric lapse rate, $\Gamma =$
 139 $-\frac{\partial T}{\partial z}$ is larger than the adiabatic lapse rate, $\frac{g}{c_p} \approx 9.5 K km^{-1}$, the atmosphere is unstable.

140 In the meantime of estimating the Brunt-Vaisala frequency, the third-order polynomial fit of the
 141 least squares has been applied to the SABER observed temperature (T) profile to estimate the
 142 background temperature (T_0) following the procedure Leblanc and Hauchecorne (1997).
 143 Succeeding the estimations of the perturbed temperature (T_p) from equation (2), the impacts of
 144 gravity waves based on the potential energy (P_E) on the mesosphere and lower thermosphere
 145 (MLT) temperature variability were identified, which is estimated by subtracting the background
 146 from the observed temperature data (T).

147
$$T_p = T - T_0 \quad (12)$$

148 After estimating the perturbed temperature (T_p), a 1-hour interval of the cut-off frequency of the
 149 low-pass band filter is used to remove the planetary and tidal wave contributions in the perturbed
 150 temperature or signal data above in one-hour time intervals to extract the impacts of a one-hour
 151 interval of gravity waves (short-periods). Then after applying the low pass band filter on the
 152 perturbed temperature (T_p), the atmospheric gravity wave of potential energy (E_p) is estimated
 153 (John and Kumar, 2012) based on the Brunt-Vaisala frequency.

154
$$E_p(z) = \frac{1}{2} \left(\frac{g(z)}{N(z)} \right)^2 \left(\frac{T_p(z)}{T_0(z)} \right)^2 \quad (13)$$

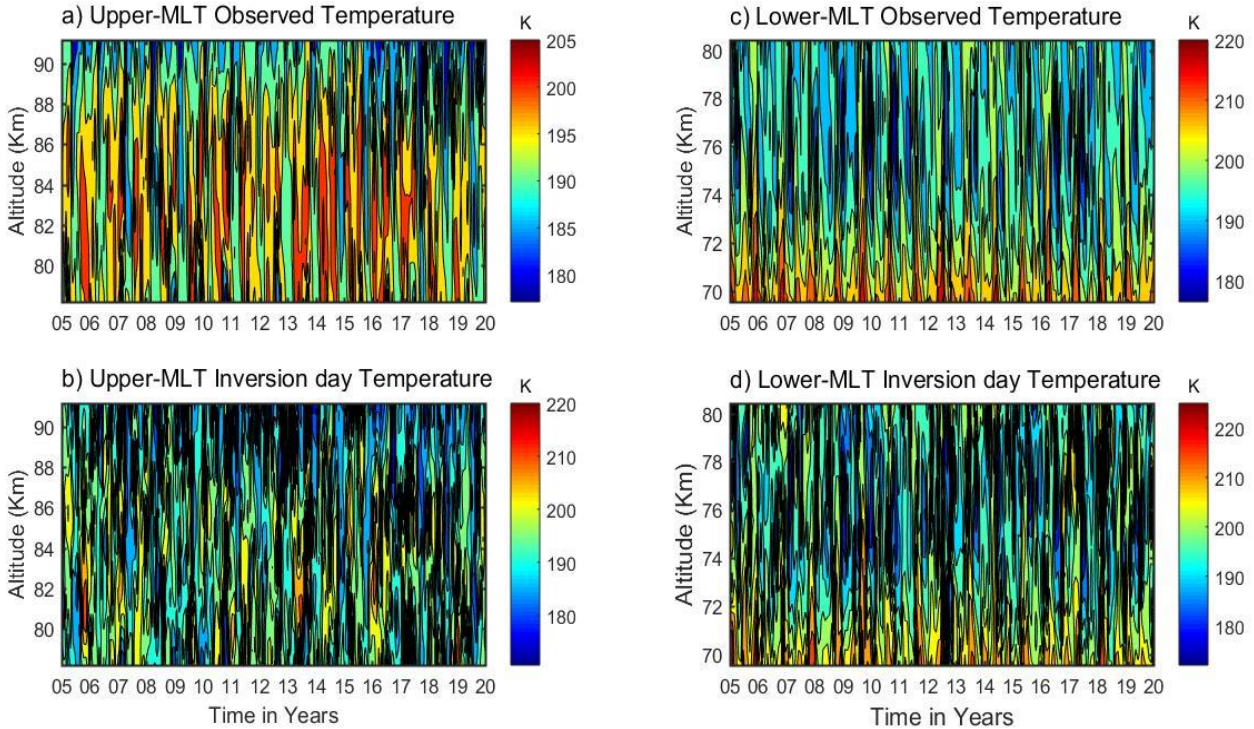
155 The potential energy of the waves is a function of altitude, z , which is utilized to determine the
 156 impact of atmospheric gravity waves on atmospheric dynamics.

157 3. Results and discussion

158 3.1 Identification and Characteristics of the Lower and Upper MLT Inversion

159 The daily SABER observed temperature profiles of the upper and lower mesospheres from 2005
 160 to 2020 over low latitudes are depicted in the form of contours in Figure 2(a and c) in the range

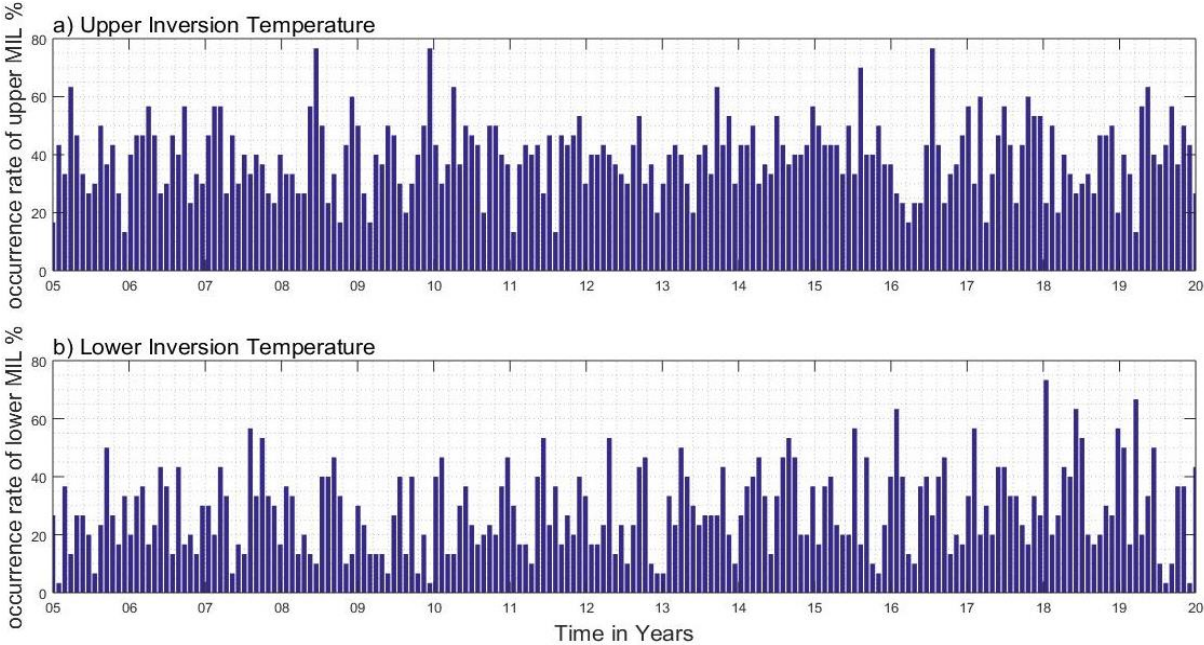
161 between \sim (180-220 K). The lower panel of Figure 2(b and d) shows daily inversion temperature
 162 profiles in the range of 180–225 K, indicating temperature is maximum in the inversion day
 163 observed temperature at lower and upper regions when compared without considering the
 164 inversion day observed temperature in Figure 2(a and c).



165 **Figure 2.** The upper and lower mesosphere observed temperatures in the first horizontal panel at
 166 (a and c) with their inversions in the second horizontal panel at (b and d).
 167

168 The upper panel on the left side of Figure 2(a) represents the upper mesosphere observed
 169 temperature, which is depicted in the range \sim (180-205 K) at the height around \sim 80-90 Km, and
 170 the right upper panel of Figure 2(c) represents the lower mesosphere observed temperature in the
 171 range around \sim (180-220 K) at the height around \sim 70-80 Km. Whereas, Figure 2(b) depicts an
 172 upper-temperature inversion about \sim (180-220 K) at an altitude of \sim (80-90 Km), while Figure 2(d)
 173 shows a lower-temperature inversion about \sim (180-225 K) at a height of \sim (70-80 Km), indicating
 174 a temperature gradient is occurred from negative to positive due to external or internal drivers,
 175 which might be atmospheric gravity waves, chemical reactions or solar radiations. The first
 176 observation of MIL was carried out by a rocket-falling experiment, which shows temperature
 177 inversion layers have been normally detected with maximum values in the mesosphere and lower
 178 thermosphere (Schmidlin, 1976). Our findings of the lower inversions in the range of (70-80 km)

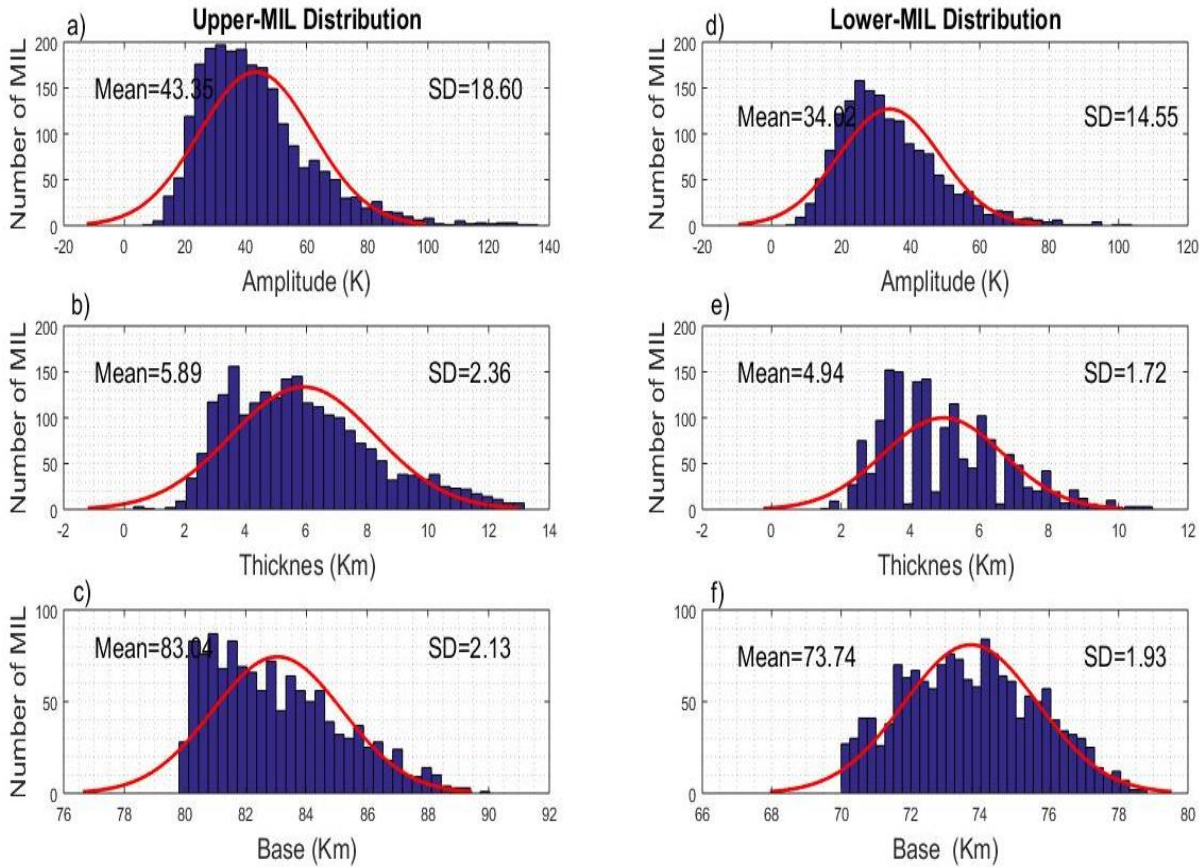
179 tend to approach the reports by Sivakumar et al. (2001), which show that the base of the lower
 180 mesospheric inversion layer (MILs) lies in the range of (73-79 km). Whereas Sivakandan et al.,
 181 (2014) also investigated the lower and upper mesospheric inversions in the altitudinal regions from
 182 60-105 km over low latitudinal regions, which nearly coincides with our work results.



183 **Figure 3.** The frequency occurrence rate (percentage) of the (a) upper and (b) lower inversion
 184 temperatures during 2005-2020 over low latitudes.
 185

186 Further, the frequency occurrence (%) of mesospheric inversion layers (MILs) is investigated
 187 during the period 2005-2020, and the results are displayed in the form of a histogram in Figure
 188 3(a) for the upper MIL and in Figure 3(b) for the lower MIL. The mean frequency occurrence rate
 189 of the upper inversion is approximately below 40%, whereas their maximum occurrence rate of
 190 inversion lies between 60% and 78%, particularly in the years 2008, 2010, and mid-2016. While
 191 the mean frequency occurrence rate of the lower inversion is below 20%. As a whole, the
 192 occurrence rate of the upper inversion is relatively high compared with the lower inversion, which
 193 could be related to atmospheric wave activities, particularly gravity wave activity. In this regard,
 194 Hauchecorne et al. (1987) and France et al. (2015) tried to show the impacts of Gws on the upper
 195 and lower mesosphere inversion variability. Not only this, Gan et al. (2012) also found the seasonal
 196 variation of MILs in the low latitudes and the causative planetary waves on the lower MILs
 197 variability. After determining the occurrence of the inversions in the lower and upper MLT
 198 regions, their consequences should be investigated.

199 Before examining the effects of Gws on the MLT regions of an inversion, Figure 4 depicts the
 200 inversions of mesosphere temperature variability in terms of base height, amplitude, and thickness.
 201 The frequency occurrence of amplitude, thickness, and base height of inversion variability in the
 202 form of the histogram along with the best-fit red lines of the Gaussian distribution are presented
 203 in Figure 4. The observed distributions coincide with Gaussian curves, indicating that the number
 204 of MILs is distributed over their attributes according to normal laws, implying that the
 205 representations are real-valued random variables. In Figure 4 of the left vertical column, three rows
 206 represent a histogram of (a) amplitude, (b) thickness, and (c) the base of the upper MIL
 207 phenomenon, along with their statistical metrics mean and standard deviations (SD). Whereas the
 208 corresponding three rows of the right vertical column represent (d) amplitude, (e) thickness, and
 209 (f) the base of the lower MIL phenomenon.



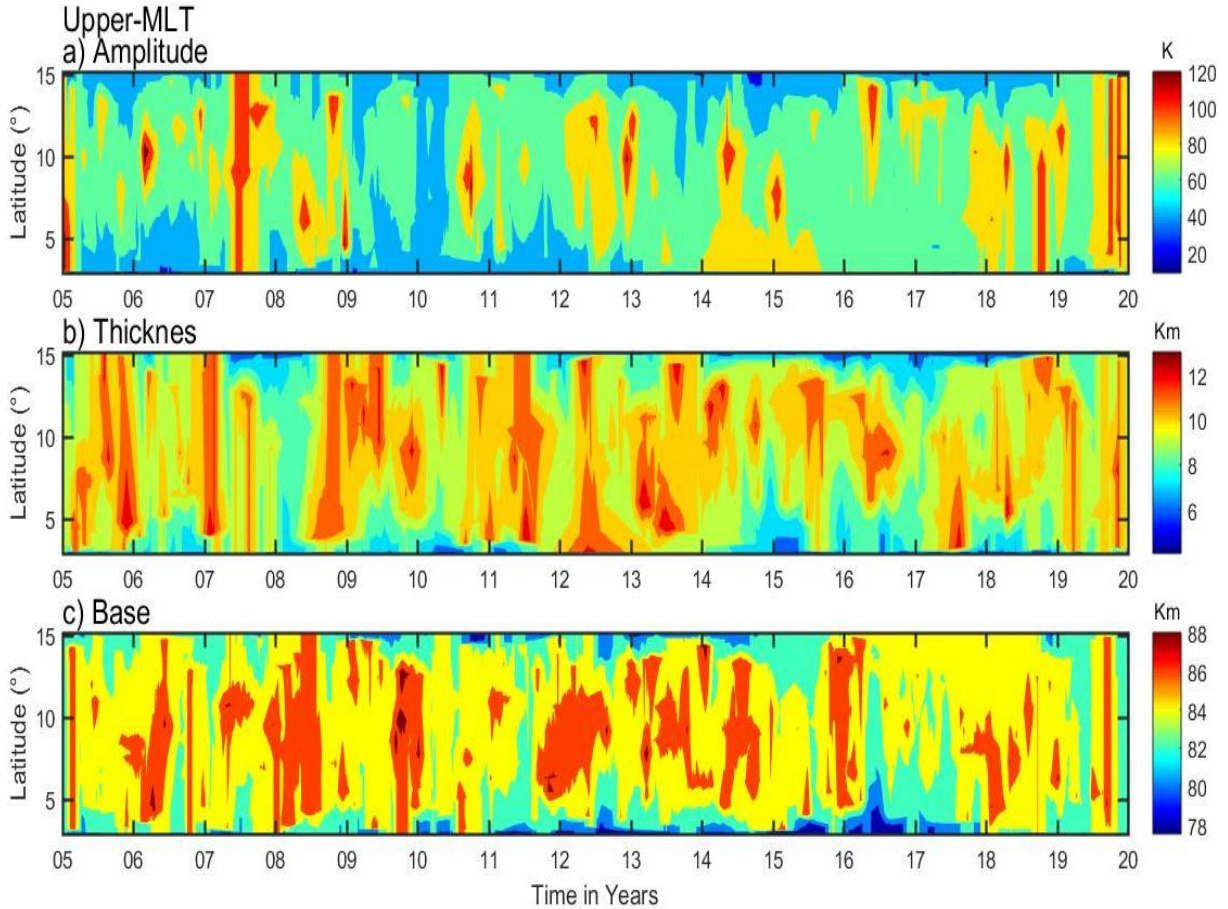
210
 211 **Figure 4.** Histogram occurrence of mesosphere inversions. The first vertical panel represents the
 212 upper inversion distribution of (a) amplitude, (b) thickness, and (c) base, and the corresponding
 213 distribution in the second vertical panel is the lower inversion of (d) amplitude, (e) thickness, and
 214 (f) base over the low latitude during the period 2005–2020.

215 The amplitude of upper inversion variability in the left vertical panel in Figure 4(a) exists in the
216 range between 20 and 80 K, with a peak value of 38 K following a Gaussian distribution with large
217 standard deviations (SD), 18.6. The thickness of the inversion layer for upper MILs has existed in
218 the range of 3-9 K, with the most probable value of 5.5 K and a low standard deviation (SD) of
219 2.3 (Figure 4(b)). The base height of the upper MIL in Figure 4(c) ranges from ~80 to 90 km, with
220 a peak value of a large number of upper mesospheric inversions occurring at a base height of
221 around 83 km in a lower standard deviation (SD) of 2.13. The number of upper inversions all over
222 the period 2005–2020 at a height of 82 km is the highest relative to the rest in the range between
223 80 and 90 km. Such maximum mean to fit of Gaussian distribution Maybe the reason for the gravity
224 wave breaking is that it dissipates energy as a causative factor for an inversion, while the wave
225 generated from the lower to the upper atmospheric region as well as the impacts of the solar flux
226 generated from the upper solar system. Whereas, the lower inversion amplitude is depicted in the
227 range between 10 and 60 K with a peak of 25 K and standard deviations (SD) of 14.5 in Figure
228 4(b) in the right vertical panel. The thickness of an inversion has appeared in the range of 3-8 Km,
229 with the most probable value of 3.8 Km and a low standard deviation (SD) of 1.72 (Figure 4(d)).
230 The base height of the lower inversion of Figure 4(f) is in the range of 70 and 80 km, with a peak
231 value of around 74 km, showing a lower standard deviation (SD) of 1.93. The statistical
232 distribution presented in this work fairly coincides with the work published by Begue et al. (2017)
233 over Reunion (20.8° S, 55.5° E) and Mauna Loa (19.5° N, 155.6° W) using Rayleigh lidar and
234 SABER observations. For both sites, MILs are found to be distributed in the altitude range of 75
235 to 82 km, with a maximum amplitude above 30K.

236 3.2 Latitudinal Variations of Mesospheric Inversion Layers (MILs)

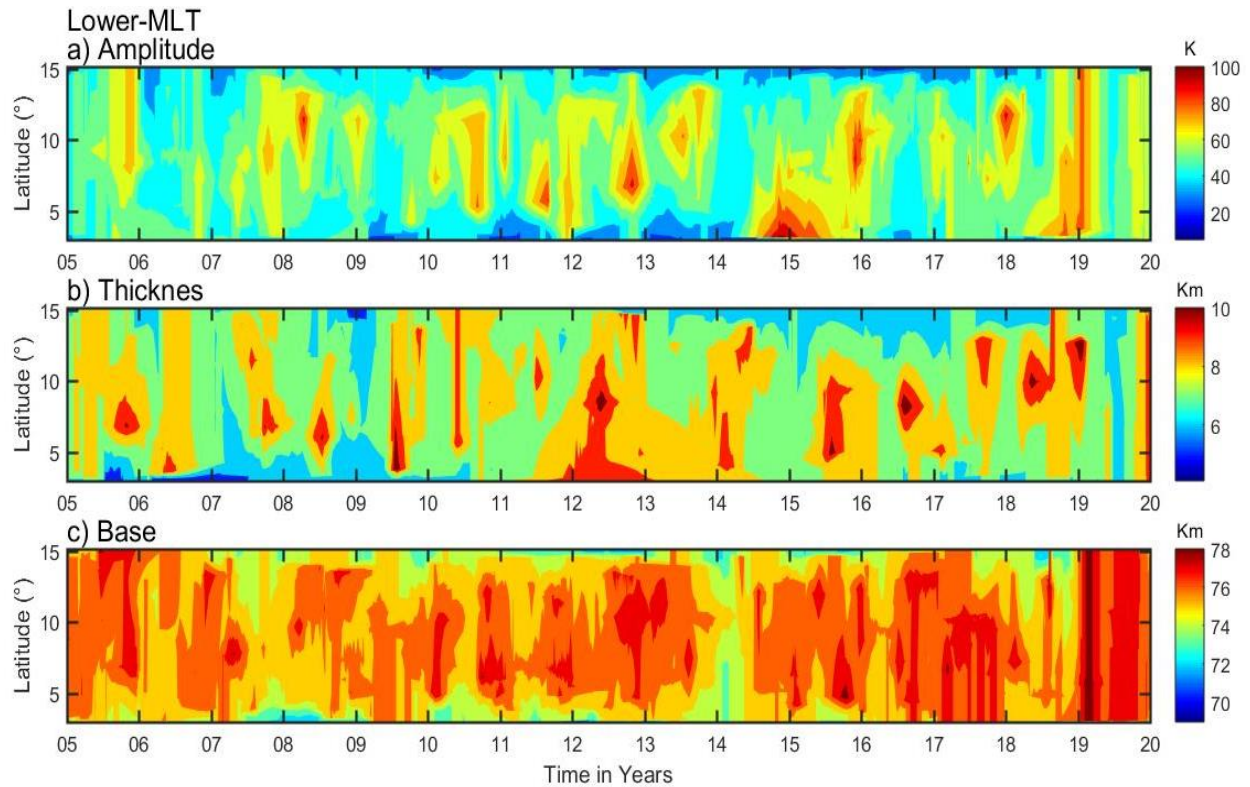
237 In this section, the spatiotemporal (latitudinal-time) variability of the upper and lower mesosphere
238 inversion phenomena is characterized in the contour plots of time vs. latitude in Figures (5 and 6)
239 respectively, based on amplitude, thickness, and base height over the low-latitude band (3-15° N)
240 during 2005–2020. The Upper MILs phenomenon is observed around 80–90 km, with the
241 maximum amplitude in the range of 90–120 K over all the latitude bands (5°-12° N) during 2005,
242 2007, mid-2011, 2013, 2015, 2016, mid-2019, and 2020 (Figure 5(a)). The inversion thickness
243 depicted in the second horizontal panel, as shown in Figure 5(b), is displayed with a maximum
244 range of ~(8–12 Km) over the entire latitudinal region (3-15° N). Figure 5(c) displays the relative

245 maximum inversion base height around $\sim(84-88 \text{ Km})$ in the latitudinal range between 4 and 14^0 N
 246 during 2006, 2008, 2010, 2012, 2016, and 2018.



247 **Figure 5.** The daily upper inversions ($\sim 80-90 \text{ km}$) of (a) amplitude, (b) thickness, and (c) base
 248 height during 2005-2020 over latitudinal variation.
 249

250 Similarly, the latitudinal variations of the lower inversion (MILs) phenomenon based on their
 251 characteristics amplitude, thicknesses, and base height are depicted in the form of contour plots of
 252 time vs latitude in Figure 6(a, b, and c), respectively, over an altitudinal range around $\sim(70-80 \text{ km})$.
 253 The lower inversion amplitude is depicted in the range of $\sim 30-60 \text{ k}$ over all latitudinal bands except
 254 the maximum range of $\sim(80-100 \text{ k})$ during 2013, 2015, 2016, and 2019 in different latitudinal
 255 regions enclosed in the range between 5 and 14^0 N . Figure 6(b) displays the inversion thickness of
 256 $5-7 \text{ km}$ over the entire latitude band, except for the maximum thickness of $8-10 \text{ km}$. The inversion
 257 of base height ($76-80$) is depicted in Figure 6(c) over all latitudes and periods except 2008, 2014,
 258 and mid-year 2018 with maximum base height. Figures 5 and 6, clearly show that the high
 259 amplitude and thickness of the upper inversion in comparison with the lower inversion indicate a
 260 highly dynamic phenomenon over the upper mesosphere region.



261 **Figure 6.** Same as Figure 5, but for the lower mesosphere inversions (~70- 80 km).
 262

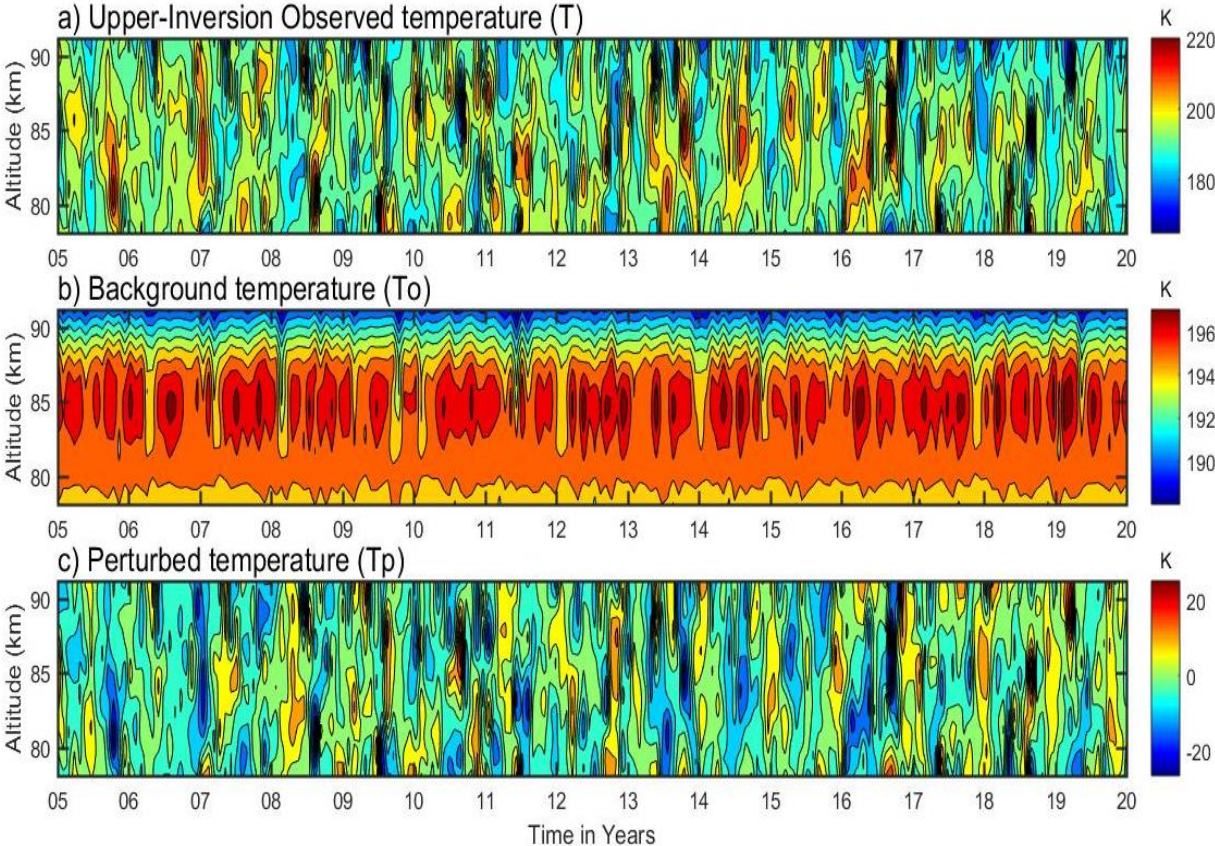
263 From Figures 5 and 6, it is observed that the upper inversion amplitude and thicknesses show high
 264 values in comparison with the lower inversion, indicating a highly dynamic phenomenon over the
 265 upper mesosphere region. Satellite measurements have a significant contribution to the
 266 information on latitudinal variations in MILs. The global climatology of MILs observed by
 267 TIMED/SABER shows that MILs also occur at low latitudes in the tropics (Gan et al., 2012).

268 3.3 Separations of the Perturbed Temperature in the Mesosphere Region

269 The perturbed temperature profiles (T_p) in the upper and lower mesosphere inversions during the
 270 period of 2005-2020 can further be used to calculate their factors' potential energy of gravity waves
 271 and the Brunt-Vaisala frequencies (N^2). The procedure for calculating perturbation temperature (T_p)
 272 is mentioned in the methodology part.

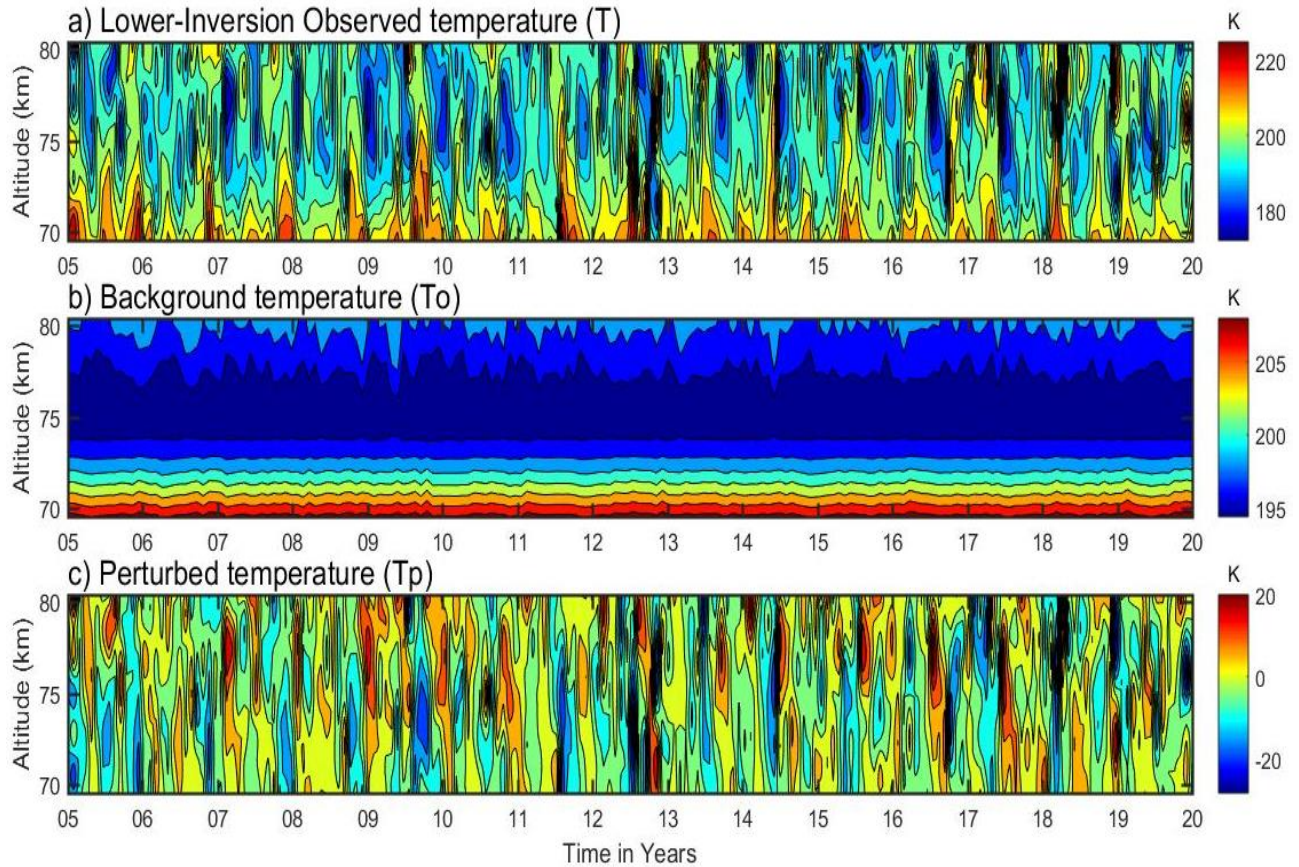
273 First, the upper-temperature inversion profiles are identified in the MLT region during the entire
 274 observational period of 2005-2020, as displayed in the contour plot of Figure 7(a). It is noted that
 275 the inversion temperature is in the range of ~170-220 K with less detectable variability. Based on
 276 this inversion temperature profile, the background temperature (T_0) is calculated by applying a 3rd-
 277 order polynomial fit as shown in the corresponding contour plot of Figure 7(b). This background

278 temperature displays identifiable periodic variability in the range of ~195-197 K around ~82-87
 279 km. While the perturbed temperature profiles (T_p) are based on the difference between the
 280 observed inversion temperature (T) and the corresponding background temperature profiles (T_o),
 281 they display in the range of -25 to +25 K, as shown in Figure 7(c).



282
 283 **Figure 7.** The upper mesosphere temperatures in the vertical panel are: (a) inversion day observed
 284 temperature; (b) background temperature; and (c) perturbed temperature in the upper mesosphere
 285 region.

286 A similar procedure has been applied to calculate the perturbed temperature (T_p) as well as the
 287 observed and background temperature from 2005 to 2020 in the lower mesosphere region, and
 288 their corresponding contours are displayed in Figure 8(a-c). The observed temperature of lower
 289 inversion in Figure 8(a) depicted a range of ~170-220 K and the background temperature of lower
 290 inversion in the range of ~ 195-210 K with their maximum values of ~200-210 K over the height
 291 of ~70-72 Km as shown in Figure 8(b). Whereas the perturbed temperature in Figure 8(c) is
 292 presented in the range between -25 and 20 K. It is noted that the upper mesosphere perturbed
 293 temperature is at its maximum compared to the lower mesosphere region, which may be due to a
 294 high dynamic phenomenon.



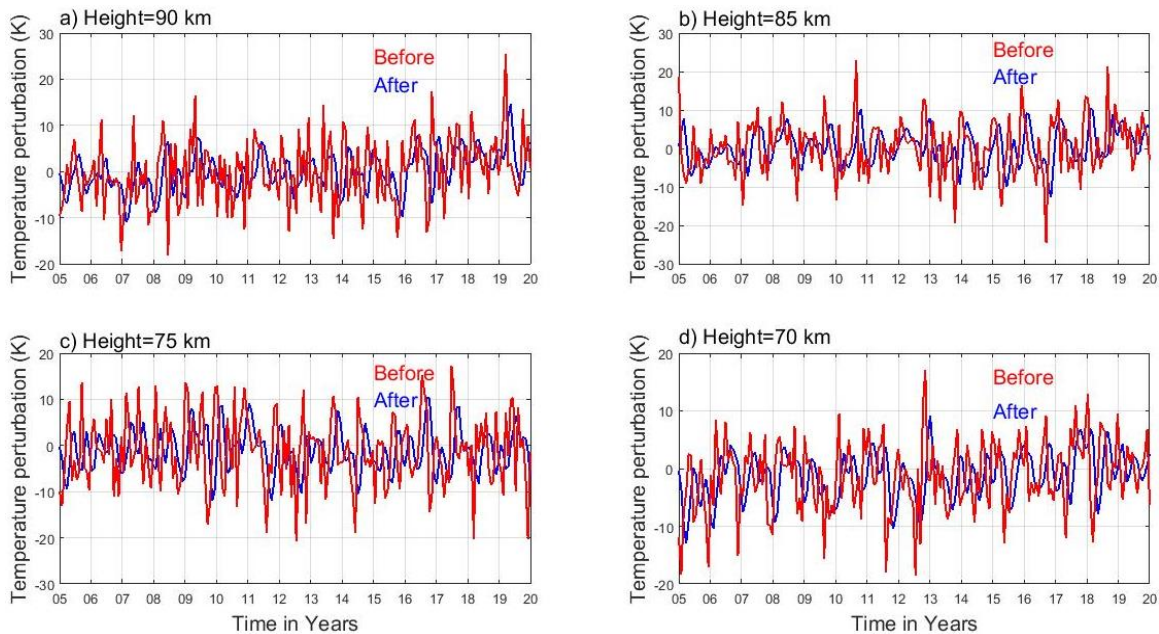
295
296 **Figure 8.** Same as Figure 7, but for the lower mesosphere atmospheric region.

297 **3.4 Effects of Gravity Waves on Mesosphere Inversions and Associated**
298 **Instability**

299 Atmospheric waves (gravity waves, planetary waves, and tidal waves) exist in different layers of
300 the atmosphere and are generated by different mechanisms. Gravity waves are of local or regional
301 dimensions, whereas the other two waves are of global extent. This dynamical influence of gravity
302 wave motion is a restoring force of gravity acting downward and buoyancy acting upward on
303 vertically displaced air parcels from the troposphere/stratosphere through the upper thermosphere.
304 These propagated gravity waves can be distributed from their source regions across the atmosphere
305 and become saturated at the critical upper atmospheric level, particularly over the low latitudes.
306 Thereby, the vertically propagated waves were breaking and dissipating to transfer their energy and
307 momentum into the atmospheric background field, thus considerably affecting the structure and
308 variability of the atmosphere, as shown in Figure 10, as well as the results of (Holton et al., 2003;
309 Holton and Hakim, 2013) waves potential energy affecting the atmospheric temperature inversions.
310 The saturation stage of the wave propagation is broken at the upper region to dissipate the energy,

311 which impacts the normal mesospheric temperature by increasing its temperature with elevation,
312 known as an inversion. This is the reason gravity wave potential energy is connected with an
313 inversion.

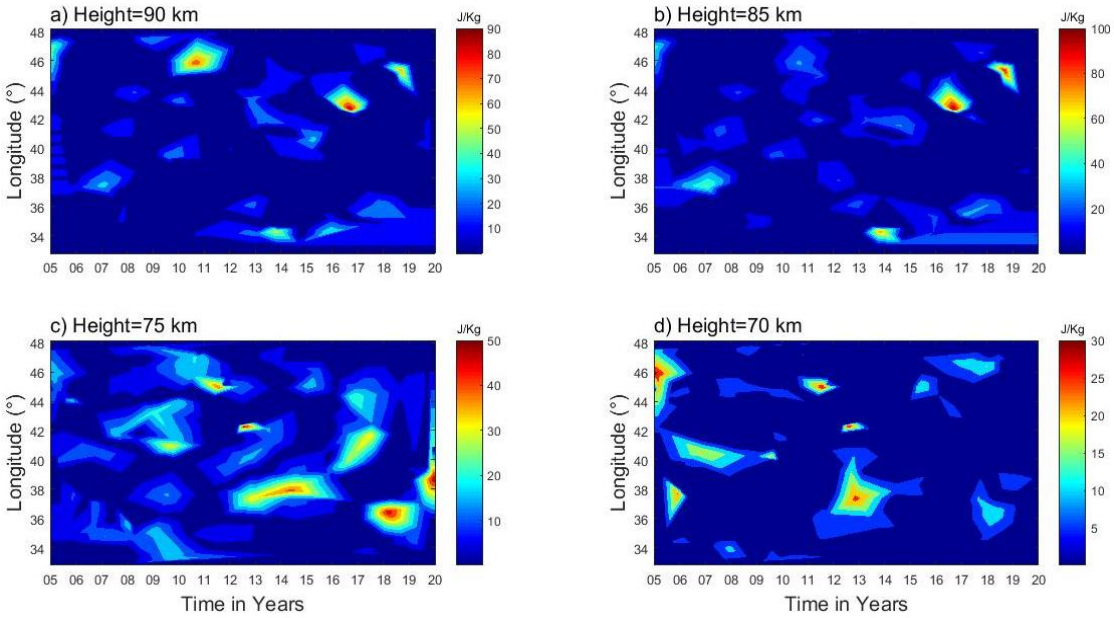
314 In this section, an attempt has been made to investigate the longitudinal variability of gravity waves'
315 contribution to the mesospheric inversions (MILs) phenomenon by calculating potential energy and
316 their instability based on Brunt-Vaisala frequency (N^2) using perturbed temperatures. Before
317 deriving the waves' potential energy from the perturbed temperature (T_p), a comparison of before
318 and after applying one-hour intervals of cut-off frequency of a low-pass band filter on a perturbed
319 temperature during the period 2005-2020 at selected heights of 90, 85, 75, and 70 km, as depicted
320 in Figure 9 (a, b, c, and d), represented by a blue line plot to remove unwanted influences on an
321 inversion. The reason behind using the low-pass band filter is to eliminate/remove the unwanted
322 influence of long-period oscillations on an inversion such as tidal or planetary waves. The effects
323 of the low-pass filter are visible before and after applying the filter in Figure 9(a and b) for the
324 upper mesosphere region at 90 and 85 km and in Figure 9(c and d) for the lower mesosphere region
325 at 75 and 70 km. The amplitude of the perturbed temperature is reduced to the range around $\sim(-10$
326 to 10 K), and the data is smoothed by eliminating higher frequencies.



327 **Figure 9.** Perturbed temperature profiles before (red color) and after (blue color) applying the low-
328 pass band filter for the upper (85 and 90 km) and lower (70 and 75 km) regions.
329

330 By using the time series of filtered perturbed temperature data at selected heights of 90, 85, 75,
331 and 70 km, the potential energy (E_p) is constructed based on the formula mentioned in the

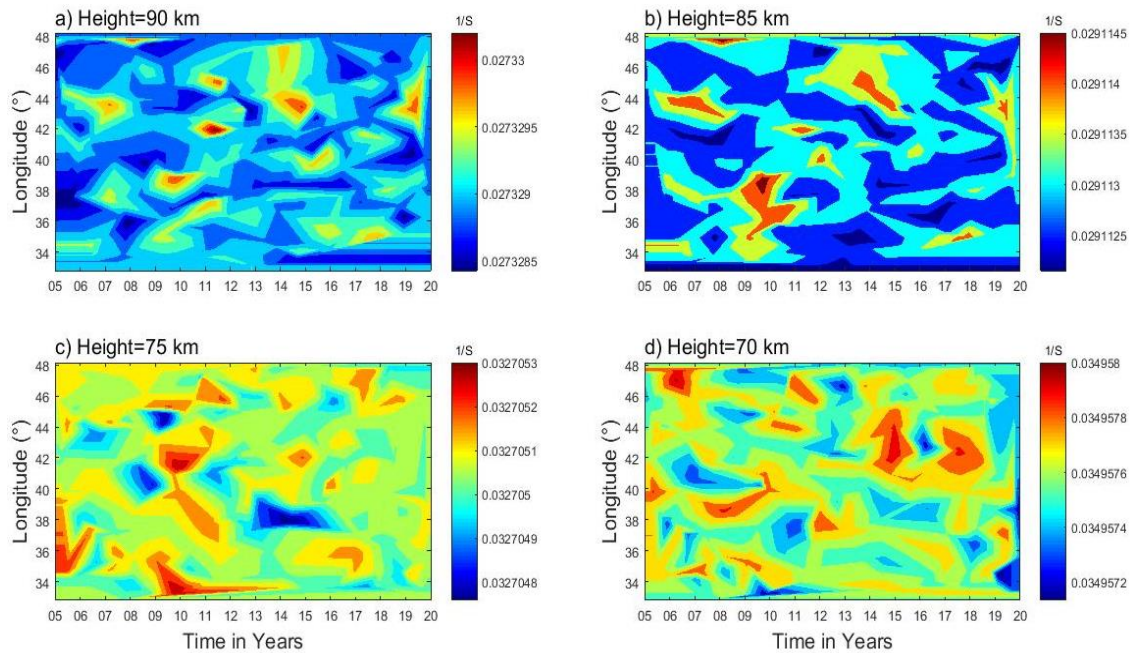
332 methodology section, since gravity wave activity is projected by potential energy calculation as
 333 described from numerous authors (Tsuda et al., 2000; Wang and Geller, 2003; Liu et al., 2014;
 334 Thurairajah et al., 2014). The spatiotemporal variability of gravity wave potential energy is shown
 335 in Figure 10(a and b) for the upper mesosphere region at (90 and 85 km) and Figure 10(c and d)
 336 for the lower mesosphere region at (75 and 70 km).



337
 338 **Figure 10.** Gravity wave potential energy for the upper (85 and 90 km) and lower (70 and 75
 339 km) mesosphere regions.

340 In this investigation, the maximum gravity wave potential energies were observed in the range of
 341 around $\sim 70\text{--}90$ J/kg over the longitudinal regions of $45\text{--}47^\circ\text{E}$, 43°E , and 44°E during 2011, 2017,
 342 and 2019 (Figure 10(a)) for upper mesosphere inversions at 90 km, whereas the low potential
 343 energy of gravity waves around $\sim 10\text{--}60$ J/kg is presented all over the longitudinal region from 33--
 344 48°E . While the maximum potential energy $\sim(70\text{--}100$ J/kg) is observed at 85 km as shown in
 345 Figure 10(b) over the longitudinal (340, 440, and 460) regions during 2014, 2016, and 2018. The
 346 low potential energy of gravity wave between 20 and 70 J/kg appears in all the longitude (33-48)
 347 regions. However, Figures 10 (c and d) show the lower mesosphere regions of gravity wave
 348 potential energy at 75 and 70 km, respectively. At a height of 75 km, a relative maximum potential
 349 energy appeared in the range of 40-50 J/kg over the longitudinal (46° , 42° , 40° , 37° , 36° , and 38°)
 350 region during 2011, 2012, 2017, 2013–2015, 2018, and 2020. Similarly, Figure 10(d) depicts the
 351 gravity wave potential energy in the range of 2–30 J/kg for the lower mesosphere region at 70 km

352 over the longitudinal region (33-48°). Out of which, the maximum potential energy of 25-30 J/kg
353 is found in a certain longitude region over a while. Many possible mechanisms have been
354 suggested for the cause of lower MIL formations, nonlinear interactions between GWs and tides
355 (Liu and Hagan, 1998), and chemical heating (Meriwether and Mlynczak, 1995) including GW
356 breaking (Hauchecorne et al., 1987). Liu et al., (2000) showed that breaking gravity waves can
357 warm the air necessary for the formation of MILs. It is also understood that gravity waves, tides,
358 planetary waves, and chemical processes are managing the middle atmospheric variability
359 (Sivakandan et al., 2014). The role of gravity wave propagation and dissipation has been accepted
360 as the dominant wave forcing in the MLT region (Lindzen, 1981; Holton, 1983), which affects the
361 middle and upper atmospheric features of an inversion. Gravity waves are multi-scale in nature;
362 small-scale waves may contribute predominantly to unstable or instability, and turbulence in the
363 MLT dynamic region (Liu and Meriwether, 2004; Szewczyk et al., 2013).
364 Hence, investigating MIL phenomena is important for the understanding of MLT atmosphere
365 dynamics for two primary reasons: stability and energy transfer. As a result, an attempt has been
366 made to examine the contributions of gravity waves to the MLT region's instability as well as the
367 MIL phenomenon using the Brunt-Vaisala frequency calculations described in the approach. The
368 spatiotemporal variability of Vaisala frequency is displayed in the contour Figure 11(a and b) for
369 the upper mesosphere region (90 and 85 km) and Figure 11(c and d) for the lower mesosphere
370 region (75 and 70 km). Based on the Brunt-Vaisala frequency, N^2 , the upper MLT region is
371 unstable (~ 0.027) at 90 km and (~ 0.029) at 85 km maximum relative to the lower inversion
372 instability at 75 km (~ 0.033) and 70 km (~ 0.035). Hauchecorne et al., (1987) described a model in
373 which a succession of breaking GWs would generate the MIL through the gradual accumulation
374 of heat as a cause of instability.



375

376 **Figure 11.** Brunt-Vaisala frequency (N^2) profiles for the upper (85 and 90 km) and lower (70
 377 and 75 km) mesosphere regions.

378 4. Summary

379 In this article, 16 years of SABER mesosphere temperature profiles are utilized to investigate the
 380 MIL phenomenon and its causative mechanism through gravity wave potential energy (P_E) and
 381 instability criteria of Brunt-Vaisala frequency (N^2) over low latitude bands. The observational
 382 conclusions from this chapter are drawn as follows:

- 383 ✓ The occurrence rate of the upper mesosphere inversion frequency is maximum relative to the
 384 mean occurrence rate of the lower mesosphere inversions.
- 385 ✓ Based on the analysis of frequency of occurrence on mesospheric inversion layer (MIL)
 386 characteristic features, it is revealed that the most probable value for upper inversion amplitude
 387 is 38 k with standard deviations (SD) of 1.72 k, inversion layer thicknesses are 5.5 km with
 388 SD of 2.3 km, and the base height is 78 km with an SD of 2.8 km. Whereas the lower inversion
 389 amplitude is 25 K with an SD of 14.5 K, the inversion layer thickness is 3.8 km with an SD of
 390 1.72 km and a base height of 73 km with an SD of 2.07 km.
- 391 ✓ The gravity wave indicator potential energy depicts high energy at the upper mesosphere
 392 region compared to the lower mesosphere region.

- 393 ✓ The result concludes that the observation of high potential energy in the upper mesosphere
394 region is due to the deposition of high energy and momentum at the background temperature
395 by gravity wave breaking, which could influence the dynamics of the inversion phenomenon
- 396 ✓ The stability criteria at the mesosphere region are indicated by Brunt-Vaisala frequency (N^2),
397 which shows low values at the upper mesosphere region relative to the lower mesosphere
398 region, leading to the conclusion that the high potential energy at the upper mesosphere region
399 is due to the instability over that region, which gives rise to large inversion phenomena.
- 400 ✓ In general, we concluded that the processes in the atmosphere vary from region to region. As
401 a result, the atmospheric state varies significantly with altitude as well as from place to place
402 and time to time.

403 **Data availability.** The SABER data are freely available via the link at [http://saber.gats-inc.com/](http://saber.gats-inc.com/index.php)
404 [index.php](http://saber.gats-inc.com/index.php).

405 **Author contribution.** Chalachew Lingerew: data curation, investigation, software, visualization,
406 writing the original draft, and writing review. U. Jaya Prakash Raju; supervision, and editing.

407 **Competing interest.** The authors declare that they have no conflict of interest relevant to this study.

408 **Acknowledgments.** The Authors would like to express their gratitude to the National Aeronautics
409 and Space Administration (NASA) for providing the SABER data downloaded from the website:
410 <http://saber.gats-inc.com/index.php>.

411 **References**

- 412 Begue, N., Mbatha, N., Bencherif, H., Loua, R. T., Siva Kumar, V., & Leblanc, T.: Statistical
413 analysis of the mesospheric inversion layers over two symmetrical tropical sites:
414 Reunion (20.8° S, 55.5° E) and Mauna Loa (19.5° N, 155.6° W). *In Annales Geophysicae*,
415 35, 1177-1194, 2017.
- 416 Bizuneh, C.L., Prakash, R., and Nigussie, M.: Long-term temperature and ozone response to natural
417 drivers in the mesospheric region using 16 years (2005–2020) of TIMED/SABER observation data
418 at 5–15°N. *Advances in Space Research*, 70, 2095–2111, [https://doi.org/10.1016/j.asr.2022.](https://doi.org/10.1016/j.asr.2022.06.051)
419 06.051, 2022.

420 Collins, R. L., Lehmacher, G. A., Larsen, M. F., and Mizutani, K.: Estimates of vertical eddy
421 diffusivity in the upper mesosphere in the presence of a mesospheric inversion layer, *Ann.*
422 *Geophys.*, 29(11), 2019–2029, <http://doi:10.5194/angeo-29-2019-2011>, 2011.

423 Cutler, L. J., Collins, R. L., Mizutani, K., and Itabe, T.: Rayleigh lidar observations of mesospheric
424 inversion layers at Poker Flat, Alaska (65° N, 14° W), *Geophys. Res. Lett.*, 28, 1467–1470,
425 <https://doi.org/10.1029/2000GL012535>, 2001.

426 Duck, T. J., Sipler, D. P., and Salah, J. E.: Rayleigh lidar observations of a mesospheric inversion
427 layer during night and day, *Geophys. Res. Lett.*, 28, 3597–3600, 2001.

428 Duck, T. J. and Greene, M. D.: High Arctic observations of mesospheric inversion layers, *Geophys.*
429 *Res. Lett.*, 31, L02105, <https://doi.org/10.1029/2003GL018481>, 2004.

430 Eckermann, S.D., Hirota, I., and Hocking, W. K.: Gravity wave and equatorial wave morphology of
431 the stratosphere derived from long-term rocket soundings. *Q. J. R. Meteorol. Soc.*, 121, 149–186,
432 <http://doi.org/10.1002/qj.49712152108>, 1994.

433 Emanuel, K.A.: *Atmospheric Convection*, Oxford University Press, New York, 580pp, 1994.

434 Fechine, J., Wrasse, C. M., Takahashi, H., Mlynczak, M. G., and Russell, J. M.: Lower-mesospheric
435 inversion layers over Brazilian equatorial region using TIMED/SABER temperature profiles, *Adv.*
436 *Space Res.*, 41, 1447–1453, <https://doi.org/10.1016/j.asr.2007.04.070>, 2008.

437 Fritts, D. C., Wang, L., Laughman, B., Lund, T. S., & Collins, R. L.: Gravity wave dynamics in a
438 mesospheric inversion layer: 2. Instabilities, turbulence, fluxes, and mixing. *Journal of*
439 *Geophysical Research: Atmospheres*, 123, 649–670, <https://doi.org/10.1002/2017JD027442>,
440 2018.

441 Fritts, D. C., and Alexander, M. J.: Gravity wave dynamics and effects in the middle atmosphere,
442 *Rev. Geophys.*, 41, 1003, <https://doi.org/10.1029/2001RG000106>, 2003.

443 Fritts, D. C., Laughman, B., Wang, L., Lund, T. S., & Collins, R. L.: Gravity wave dynamics in a
444 mesospheric inversion layer: 1. Reflection, trapping, and instability dynamics. *Journal of*
445 *Geophysical Research: Atmospheres*, 123, 626–648, <https://doi.org/10.1002/2017JD027440>, 2018.

446 Gan, Q., Zhang, S. D., and Yi, F.: TIMED/SABER observations of lower mesospheric inversion
447 layers at low and middle latitudes, *J. Geophys. Res.*, 117, D07109, <https://doi:10.1029/2012JD>
448 017455, 2012.

449 Garcia-Comas, M., Lopez-Puertas, M., Marshall, B. T., Winter Steiner, P. P., Funke, B., Bermejo-
450 Pantaleon, D., Mertens, C. J., Remsberg, E. E., Gordley, L. L., Mlynczak, M. G., and Russell III,

451 J. M.: Errors in Sounding of the Atmosphere using Broadband Emission Radiometry (SABER)
452 kinetic temperature caused by non-local-thermodynamic-equilibrium model parameters, J.
453 Geophys. Res., 113, D24106, doi: 10.1029/2008JD010105, 2008.

454 Hirota, I.: Climatology of gravity waves in the middle atmosphere. J. Atmos. Terr. Phys., 46, 767–
455 773, <http://doi.org/10.2151/jmsj1965.63.6-1055>, 1984.

456 Hamilton, K.: Climatological Statistics of Stratospheric Inertia-Gravity Waves Deduced from
457 Historical Rocket-sonde Wind and Temperature Data. J. Geophys. Res., 96, 20831–20839,
458 <http://doi.org/10.1029/91JD02188>, 1991.

459 Hauchecorne, A., Chanin, M. L., & Wilson, R.: Mesospheric temperature inversion and
460 gravity wave breaking. *Geophysical Research Letters*, 14(9), 933-936, [https://doi.org/10.1029/
461 GL014i009p00933](https://doi.org/10.1029/GL014i009p00933), 1987.

462 Holton, J. R., Curry, J. A., and Pyle, J. A.: *Encyclopedia of atmospheric sciences*, volume 1.
463 Academic Press, 2003.

464 Holton, J. R.: The influence of gravity wave breaking on the general circulation of the middle
465 atmosphere, J. Atmos. Sci., 40, 2497–2507, 1983.

466 Holton, J. R. and Hakim, G. J.: *An introduction to dynamic meteorology*. Academic Press, 2013.

467 Irving, B. K., Collins, R. L., Lieberman, R. S., Thurairajah, B., and Mizutani, K.: Mesospheric
468 Inversion Layers at Chatanika, Alaska (65°N, 147°W): Rayleigh lidar observations and analysis,
469 J. Geophys. Res. Atmos., 119, 11,235–249, <http://doi:10.1002/2014JD021838>, 2014.

470 John, S.R., Kumar, K. K.: TIMED/SABER observations of global gravity wave climatology and
471 their interannual variability from stratosphere to mesosphere lower thermosphere. *Clim. Dyn.*, 39,
472 1489–1505, <http://doi.org/10.1007/s00382-012-1329-9>, 2012.

473 Leblanc, T., McDermid, I. S., Hauchecorne, A., and Keck hut, P.: Evaluation of optimization of lidar
474 temperature analysis algorithms using simulated data, J. Geophys. Res., 103, 6177–6187, 1998.

475 Leblanc, T., and Hauchecorne, A.: Recent observations of mesospheric temperature inversions, J.
476 Geophys. Res., 102, 19471–19482, <https://doi.org/10.1029/97JD01445>, 1997.

477 Lindzen, R. S.: Turbulence and stress due to gravity waves and tidal breakdown, J. Geophys. Res.,
478 86, 9707–9714, <https://doi:10.1029/JC086iC10p09707>, 1981.

479 Lingerew, C., Jaya Prakash Raju, U., & Guimarães Santos, C. A.: NN-MLT model prediction for
480 low-latitude region based on artificial neural network and long-term SABER observations. *Earth
481 and Space Science*, 10, e2023EA002930, <https://doi.org/10.1029/2023 EA002930>, 2023.

482 Liu, S-D., and S-S. Liu: *Atmosphere Dynamics*, Peking University Press, Beijing, 2011.

483 Liu, H. L., Hagan, M. E., & Roble, R. G.: Local mean state changes due to gravity wave
484 breaking modulated by the diurnal tide. *Journal of Geophysical Research*, 105(D10),
485 12381-12396, (2000).

486 Liu, H. L., & Hagan, M. E.: Local heating/cooling of Atmospheres. 96(D8), 15297-15309, (1998).

487 Mlynczak, M. G., Marshall, B. T., Martin-Torres, F. J., Russell III, J. M., Thompson, R. E.,
488 Remsberg, E. E., and Gordley, L. L.: Sounding of the Atmosphere using Broadband Emission
489 Radiometry observations of daytime mesospheric O₂ (1Δ) 1.27 μm emission and derivation of
490 ozone, atomic oxygen, and solar and chemical energy deposition rates, 2007.

491 Meriwether, J. W., and Gerrard, A. J.: Mesosphere inversion layers and stratosphere temperature
492 enhancements, *Rev. Geophys.*, 42, RG3003, <http://doi:10.1029/2003RG000133>, 2004.

493 Meriwether, J. W., and Gardner, C. S.: A review of the mesosphere inversion layer phenomenon, *J.*
494 *Geophys. Res.*, 105, 12 405–12 416, 2000.

495 Nath, O., & Sridharan, S.: Long-term variabilities and tendencies in zonal mean TIMED–SABER
496 ozone and temperature in the middle atmosphere at 10–15°N. *Journal of Atmospheric and Solar-*
497 *Terrestrial Physics*, 120, 1–8, <https://doi:10.1016/j.jastp.2014.08.010>, 2014.

498 Ramesh, K., Sridharan, S.: Large mesospheric inversion layer due to breaking of small scale gravity
499 waves: Evidence from Rayleigh lidar observations over Gadanki (13.51⁰ N, 79.21⁰ E). *J. Atmos.*
500 *Sol. Terr. Phys.* 89, 90–97, <http://doi.org/10.1016/j.jastp.2012.08.011>, 2012.

501 Ramesh, K., Sridharan, S. and Vijaya Bhaskara, S.: Causative mechanisms for the occurrence of a
502 triple-layered mesospheric inversion event over low latitudes, *J. Geophys. Res. Space Physics*,
503 119, 3930–3943, <http://doi:10.1002/2013JA019750>, 2014.

504 Ramesh, K., Sridharan, S., Raghunath, K., and Rao, S. V. B.: A chemical perspective of day and
505 night tropical (10°N–15°N) mesospheric inversion layers, *J. Geophys. Res. Space Physics*, 122,
506 <http://doi:10.1002/2016JA023721>, 2017.

507 Ramesh, K., Sridharan, S., Vijaya Bhaskara Rao, S., Raghunath, K., Bhavani Kumar, K.: Rayleigh
508 lidar observations of mesospheric inversion layers over Gadanki (13.5⁰N, 79.2⁰ E) and their
509 relation with gravity wave activities. *Indian Journal of Radio and Space Science*, 43, 83-90, 2013.

510 Remsberg, E., Lingenfelter, V., Harvey, V., Grose, W., Russell III, J., Mlynczak, M., Gordley, L.,
511 and Marshall, B. T.: The verification of the quality of SABER temperature, geopotential height,

512 and wind fields by comparison with Met Office assimilated analyses, *J. Geophys. Res.*, 108(D19),
513 4628, <https://doi.org/10.1029/2003JD003720>, 2003.

514 Rezac, L., Kutepov, A., Russell, J.M., Feofilov, A.G., Yue, J., and Goldberg, R.A.: Simultaneous
515 retrieval of T (p) and CO₂ VMR from two-channel non-LTE limb radiances and application to
516 daytime SABER/ TIMED measurements. *J. Atmos. Sol. Terr. Phys* 130–131, 23–42.
517 <https://doi.org/10.1016/j.jastp.2015.05.004>, 2015.

518 Russell, J.M., Mlynczak, M.G., Gordley, L.L., Tansock, J., Esplin, R.: An overview of the SABER
519 experiment and preliminary calibration results. In *Proceedings of the SPIE, 44th Annual Meeting*,
520 Denver, CO, USA, 3756, 277–288, 1999.

521 Schmidlin, F. J.: Temperature inversions near 75 km. *Geophysical Research Letters*, 3(3),
522 173-176, (1976).

523 Sica, R. J., Argall, P. S., Shepherd, T. G., and Koshyk, J. N.: Model-measurement comparison of
524 mesospheric temperature inversions, and a simple theory for their occurrence, *Geophys. Res. Lett.*,
525 34, L23806, <https://doi.org/10.1029/2007GL030627>, 2007.

526 Sivakandan, M., Kapasi, D., and Taori, A.: The occurrence altitudes of middle atmospheric
527 temperature inversions and mesopause over low-latitude Indian sector, *Ann. Geophys.*, 32,
528 967–974, <https://doi.org/10.5194/angeo-32-967-2014>, 2014.

529 Siva Kumar, V., Bhavani Kumar, Y., Raghunath, K., Rao, P. B., Krishnaiah, M., Mizutani, K., Aoki,
530 T., Yasui, M., and Itabe, T.: Lidar measurements of mesospheric temperature inversion at a low
531 latitude, *Ann. Geophys.*, 19, 1039–1044, <https://doi.org/10.5194/angeo-19-1039-2001>, 2001.

532 Sridharan, S., Sathishkumar, S., and Gurubaran, S.: Influence of gravity waves and tides on
533 mesospheric temperature inversion layers: simultaneous Rayleigh lidar and MF radar
534 observations, *Ann. Geophys.*, 26, 3731–3739, 2008.

535 Singh, R. P., & Pallamraju, D.: Mesospheric temperature inversions observed in OH and O₂
536 rotational temperatures from Mount Abu (24.6°N, 72.8°E), India. *Journal of Geophysical*
537 *Research: Space Physics*, 123, 8823–8834, <https://doi.org/10.1029/2018JA025703>, 2018.

538 Smith, A.: Global Dynamics of the MLT, *Surv. Geophys*, 33, 1177–1230, <https://doi.org/10.1007/s10712-012-9196-9>, 2012.

540 Szewczyk, A., Strelnikov, B., Rapp, M., Strelnikova, I., Baumgarten, G., Kaifler, N., Dunker, T.,
541 and Hoppe, U. P.: Simultaneous observations of a Mesospheric Inversion Layer and turbulence

542 during the ECOMA-2010 rocket campaign, *Ann. Geophys.*, 31, 775–785, [http://doi:10.5194/](http://doi:10.5194/angeo-31-775-2013)
543 [angeo-31-775-2013](http://doi:10.5194/angeo-31-775-2013), 2013.

544 Vadas, S. L., and Fritts, D. C.: Thermosphere responses to gravity waves: Influences of increasing
545 viscosity and thermal diffusivity, *J. Geophys. Res.*, VOL. 110, D15103, doi: 10.1029/2004JD
546 005574, 2005.

547 Wang, L., Geller, M.A., Alexander, M.J.: Spatial and Temporal Variations of Gravity Wave
548 Parameters. Part I: Intrinsic Frequency, Wavelength, and Vertical Propagation Direction. *J. Atmos.*
549 *Sci.*, 62, 125–142, <http://doi.org/10.1029/2010JD013860>, 2005.

550 Wang, L., and Alexander, M.J.: Global estimates of gravity wave parameters from GPS radio
551 occultation temperature data. *J. Geophys. Res.* 115, D21122, [http://doi.org/10.1029/2010J](http://doi.org/10.1029/2010JD013860)
552 [D013860](http://doi.org/10.1029/2010JD013860), 2010.

553 Walterscheid, R. L., and Hickey, M. P.: Gravity wave ducting in the upper mesosphere and lower
554 thermosphere duct system, *J. Geophys. Res.*, 114, D19109, [http://doi:10.1029/2008JD 011269](http://doi:10.1029/2008JD011269),
555 2009.

556 Yuan, T., Pautet, P. D., Zhao, Y., Cai, X., Criddle, N. R., Taylor, M. J., and Pendleton, W. R.:
557 Coordinated investigation of mid-latitude upper mesospheric temperature inversion layers and the
558 associated gravity wave forcing in Logan, Utah, *J. Geophys. Res. Atmos.*, 119, 3756–3769,
559 <http://doi:10.1002/2013JD020586>, 2014.